LIMNOLOGY
and
OCEANOGRAPHY

ASLO

Limnol. Oceanogr. 63, 2018, 2545–2562

doi: 10.1002/lno.10959

High-turbidity events in Western Lake Erie during ice-free cycles: Contributions of river-loaded vs. resuspended sediments

Qianru Niu,[1,2] Meng Xia ,[2*] Stuart A. Ludsin,[3] Philip Y. Chu,[4] Doran M. Mason,[4] Edward S. Rutherford[4]

[1]Shenzhen Key Laboratory of Marine Bioresource and Eco-Environmental Sciences, Shenzhen Engineering Laboratory for Marine Algal Biotechnology, College of Life Sciences and Oceanography, Shenzhen University, Shenzhen, People's Republic of China
[2]Department of Natural Sciences, University of Maryland Eastern Shore, Princess Anne, Maryland
[3]Aquatic Ecology Laboratory, Department of Evolution, Ecology and Organismal Biology, The Ohio State University, Columbus, Ohio
[4]NOAA Great Lakes Environmental Research Laboratory, Ann Arbor, Michigan

Abstract

High-turbidity events (HTEs) are common phenomena in shallow-water environments that can alter ecological interactions. The relative contributions of river input (external loading) vs. resuspension (internal loading) to the occurrence, duration, and influenced areas of HTEs are not fully understood in most systems, owing to the lack of long-term, source-specified sediment maps. Using a Finite Volume Community Ocean Model-based wave-current forced sediment model, we investigated sediment dynamics in the shallow, river-dominated Western Lake Erie during ice-free cycles (April–November) of 2002–2012. Results indicated that wind waves predominated sediment dynamics in the offshore areas, with river discharges causing substantial inshore to offshore gradients. Owing to varying wind waves and river discharges, both the mean and extreme sediment dynamics had distinctive seasonal variations. The basin was turbid during spring and fall, with frequent (> 15%), broad (O [10^2–10^3 km^2]), and more persistent (means of 3.2/4.4 d during spring/fall) HTEs caused mainly by resuspension events. During summer, the basin was clearer with occasional (< 1%), small (O [1–10^2 km^2]), and short (mean of 1.5 d) HTEs near the mouths generated by pulsing river loadings. Although river loading rarely induced basin-wide HTEs, they were important during floods, enlarging the high-turbidity areas by 11.3%. Overall, by delineating the drivers of HTEs in Western Lake Erie, this study furthered the understanding of sediment dynamics in shallow ecosystems and provides a basis for investigating the ecological impact of sediments from different sources in river- and wave-energetic systems.

The food webs and fisheries of large lakes and coastal ecosystems are fragile and have been threatened by both sediment and nutrient pollutions (Carpenter et al. 1998; Islam and Tanaka 2004; Rabalais et al. 2014; Sterner et al. 2017). To protect the biota in these ecosystems, as well as to understand their dynamics, effort has been devoted to develop state-of-the-art ecological models (e.g., Ludsin et al. 2014; Jiang et al. 2015; Xia and Jiang 2016). The accuracy of these models depends on the understanding of the mechanisms that drive both biological and physical processes. In large lakes and coastal ecosystems, achieving this understanding has been limited by an inability to correctly model suspended sediment dynamics, which can play an important role in driving biogeochemical and ecological processes, especially during high-turbidity events (HTEs; e.g., Reichert et al. 2010; Carey and Rydin 2011; Moriarty et al. 2017; Paytan et al. 2017).

Given the importance of suspended sediments, their dynamics have been extensively investigated. Initially, field observations and laboratory experiments were conducted to understand sediment erosion, deposition, and transport (e.g., Fukuda and Lick 1980; Mehta 1986; Harris et al. 2008). Later, satellite images have been used to capture the spatial patterns of turbidity plumes during cloud-free days (e.g., Schwab et al. 2000; Shen et al. 2013), indicating the likely role that river discharge and wind played in driving HTEs. With the availability of long term, continuous satellite observations and increasing effort to model sediment dynamics, the importance of external forcing (wind and river discharge) in dominating their seasonal variations has been recognized (e.g., Chen et al. 2007; Saldías et al. 2012; Mendes et al. 2017), and the impacts of suspended sediments on ecosystem and ecological dynamics have been assessed (e.g., Grimes and Finucane 1991; Reichert et al. 2010; Le

*Correspondence: mxia@umes.edu

et al. 2013). Despite previous studies shed light on sediment plume dynamics on multiple temporal scales, the origins of the sediments in these turbid plumes remain unclear.

In river-dominated, shallow-water ecosystems, the majority of suspended sediments originate externally from river loading and internally from resuspension (Fig. 1a). River plumes are driven by river discharge, wind, and the Earth's rotation collectively (Xia et al. 2011; Jiang and Xia 2016). As the river-loaded sediments carry nutrients and contaminants from their watersheds, the generated plumes influence the heterogeneity in biological productivity and species interactions/migrations (Grimes and Kingsford 1996; Carreon-Martinez et al. 2014; Xia et al. 2016; Wu et al. 2017). Resuspension is initiated by the combined effects of currents, surface-gravity waves, and high-frequency linear internal waves, among which the surface-gravity waves predominate in shallow lakes and coastal zones (Hawley and Eadie 2007; Green and Coco 2014; Valipour et al. 2017). During the resuspension, resuspended materials can alter the biomass distributions by reintroducing and redistributing nutrients throughout the water column (Zamparas and Zacharias 2014; Dong et al. 2015, 2016; Paytan et al. 2017; Li et al., 2018), which in turn can impact the dissolved oxygen levels (Moriarty et al. 2017). Given that suspended sediments from river loading and resuspension have distinct ecological functions and driving mechanisms, it is critical to understand their relative contributions to HTEs by tracking their origins explicitly. At present, however, this understanding cannot be fulfilled through field or satellite observations (e.g., Saldías et al. 2012; Mendes et al. 2017; Valipour et al. 2017), nor has it been sufficiently investigated thoroughly in the modeling studies that have been conducted to date (e.g., Lou et al. 2000; Liu and Wang 2014; Morales-Marin et al. 2017; Yellen et al. 2017).

To understand the contributions of river loading and resuspension to HTEs, a state-of-the-art wave-current forced sediment model was developed in Western Lake Erie (U.S.A.-Canada). The basin is a river-dominated, wave-energetic ecosystem (Bolsenga and Herdendorf 1993) and the roles of HTEs in ecological interactions are only just beginning to be understood (Reichert et al. 2010; Carreon-Martinez et al. 2014; Ludsin et al. 2014). The main objectives of the present study are as follows: (1) to understand the driving factors of suspended sediment dynamics in Western Lake Erie; (2) to investigate the seasonal variations in the basin's mean and extreme suspended sediment dynamics; and (3) to discuss the relative contributions of river loading vs. resuspension to HTEs' occurrence, duration, and influenced area on the seasonal scale, as well as during floods.

The outline of the article is as follows. First, the study area and coupled modeling system are introduced, following the model's validation and skill assessment. Then, dynamics and variations of suspended sediments, as well as the relative contributions of river loading and resuspension to HTEs, are discussed, with the major conclusions and perspectives for future research summarized in "Conclusions" section. Acronyms and notations used in the following sections are listed in Table 1.

Methodology

Study area: Western Lake Erie

Lake Erie's western basin is the smallest (3284 km^2) and shallowest (mean depth of ~ 7.4 m) of its three basins, receiving a more than 5000 m^3 s^{-1} of discharge from the five surrounding tributaries (Fig. 2). The Detroit and Maumee rivers historically have contributed the majority of momentum, nutrients, and sediments into the lake (Bolsenga and Herdendorf 1993; Table 2). Detroit River discharge accelerates eastward inter-basin transport by interacting with wind-induced currents (Niu et al. 2015). The Maumee River is the major

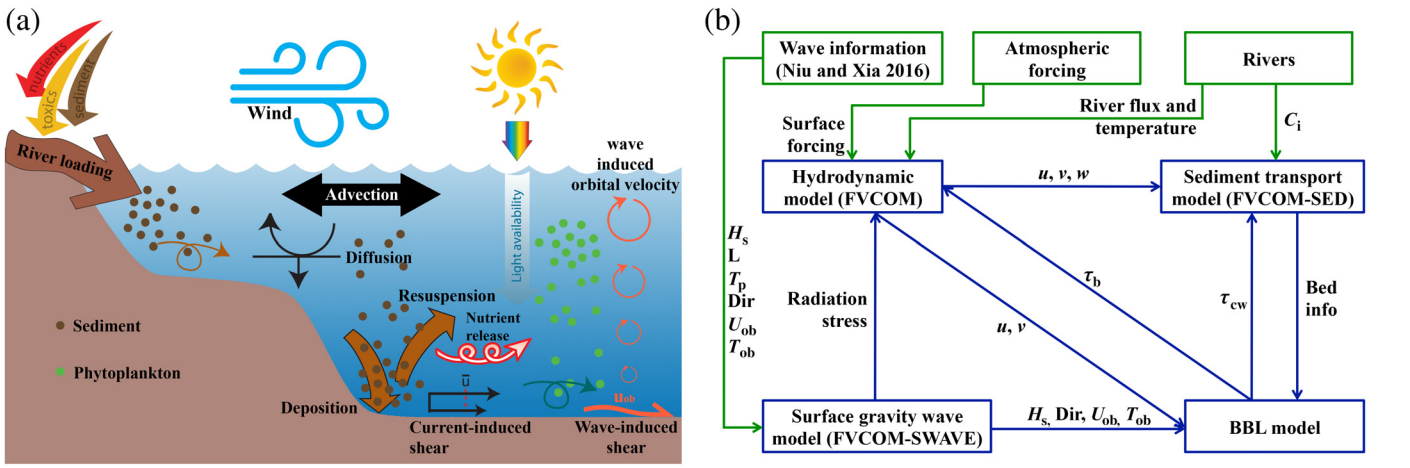

Fig. 1. (**a**) Conceptual diagrams of suspended sediments in shallow-water environments. (**b**) The external forcing and coupling between the wave (FVCOM-SWAVE), current (FVCOM), and sediment (FVCOM-SED) models through the BBL model with notes of the exchanged data. Notations are listed in Table 1.

Table 1. List of acronyms and notations.

Symbol	Description
m_i	Annual sediment loading from river *i*
r	Pearson correlation coefficient
u, v, w	Current velocities in the x, y, and z directions
w_s	Settling velocity
τ_b	Mean bottom stress due to combined waves and currents
τ_c	Bottom stress due to currents
τ_{cd}	Critical bottom stress for sediment deposition
τ_{ce}	Critical bottom stress for sediment erosion
τ_{cw}	Maximum instantaneous bottom stress by representative waves and currents
τ_w	Bottom stress due to waves
BBL	Bottom boundary layer
C	Sediment concentration
Dir	Wave direction
E	Erosion rate constant
F_i	Discharge of river *i*
F_{DE}	Detroit River discharge
F_{MA}	Maumee River discharge
FVCOM	Finite Volume Community Ocean Model
H_s	Significant wave height
HTEs	High-turbidity events (SSC > 30 mg L^{-1})
L	Wavelength
P_{bias}	Percentage bias
RMSD	Root-mean-square deviation
SSC	Surface sediment concentration
T_p	Relative peak wave period
T_{ob}	Bottom wave period
TSS	Total sediment concentration
U_{ob}	Bottom orbital velocity
U_{wnd}	Wind speed at 10 m above ground

contributor of nutrients, and it generates significant inshore to offshore gradients in biological processes and species interactions at its river mouth (Schwab et al. 2009; Reichert et al. 2010; Jiang et al. 2015).

The meteorological forcing and river discharges have distinctive seasonality in the western basin. The basin is dominated by strong northeast winds with southward waves during spring, weak wind and waves with various directions during summer, and southwest gusts with intense northeastward waves during fall (Fig. 3a,b). Both the mean and 95th percentile Detroit River discharge have limited seasonal variations (Fig. 3c), whereas discharges from the other inflows (Maumee, Sandusky, Raisin, and Portage rivers) are high during spring and low during summer and fall (Fig. 3d,e).

The wave-current forced sediment model

The sediment model in Western Lake Erie was configured based on an unstructured-grid three-dimensional (3D) sediment transport model (FVCOM-SED, i.e., Finite Volume Community Ocean Model-Sediment). The sediment model was driven by a wave-current coupled modeling system developed by Niu and Xia (2017), which is based on the lake's hydrodynamic (FVCOM; Niu et al. 2015) and wave (FVCOM-SWAVE, i.e., FVCOM Surface Wave; Niu and Xia 2016) models. FVCOM adopts unstructured triangle grids horizontally and sigma coordinates vertically, which allow it to follow coastlines and bathymetry. FVCOM-SWAVE is a third-generation wave model, and it comprises the shallow-water wave characteristics by solving the wave-action spectral energy balance equation. The model implements a flux-corrected transport algorithm and an implicit Crank–Nicolson solver in the wave frequency and direction spaces, respectively, with a finite-volume solver in the geographic space. The Lake Erie wave model (Niu and Xia 2016) resolved wave spectral frequency range from 0.04 Hz to 1.0 Hz (with 10 frequency bins) and applied a full cycle (0°–360°) direction spectrum (with 36 direction bins). It applied the exponential wave growth and whitecapping function according to Janssen (1989, 1991), and the Madsen bottom friction model is utilized.

FVCOM-SED is an unstructured-grid 3D sediment transport module included in FVCOM. It is based on the United States Geological Survey (USGS) Community Sediment Transport Model and has been applied in coastal regions and large lakes (e.g., Ge et al. 2015; Morales-Marin et al. 2017; Yellen et al. 2017). The model includes suspended and bedload sediment transport, layered bed dynamics based on the active layer concept, flux-limited solution of sediment settling, unlimited number of sediment classes and bed layers and cohesive sediment erosion/deposition algorithms. Suspended sediments transport is governed by a 3D advection–diffusion equation, given as

$$\frac{\partial C_i}{\partial t}+\frac{\partial uC_i}{\partial x}+\frac{\partial vC_i}{\partial y}+\frac{\partial (w-w_{si})C_i}{\partial z} = \frac{\partial}{\partial x}\left(A_h\frac{\partial C_i}{\partial x}\right)+\frac{\partial}{\partial y}\left(A_h\frac{\partial C_i}{\partial y}\right)+\frac{\partial}{\partial z}\left(K_h\frac{\partial C_i}{\partial z}\right) \quad (1)$$

where (u, v, w) are the velocity components in the (x, y, z) directions, respectively; C_i and w_{si} are the concentration and settling velocity of sediment i, respectively; and A_h and K_h are the horizontal and vertical eddy viscosities, respectively.

The wave-current coupled modeling system incorporated the wave-induced excessive fluxes of momentum (radiation stress) as Mellor (2015). Meanwhile, an advanced bottom boundary layer (BBL) model was applied to calculate the wave-current boundary layer bottom stress. The model utilizes the two-layer eddy viscosity method of Madsen (1994), with roughness calculated internally as a function of the grain roughness, sediment transport, and bedform roughness length. The sediment (FVCOM-SED) model was driven by the wave-current coupled modeling system through the consideration of following forcing factors: (1) currents and turbulences

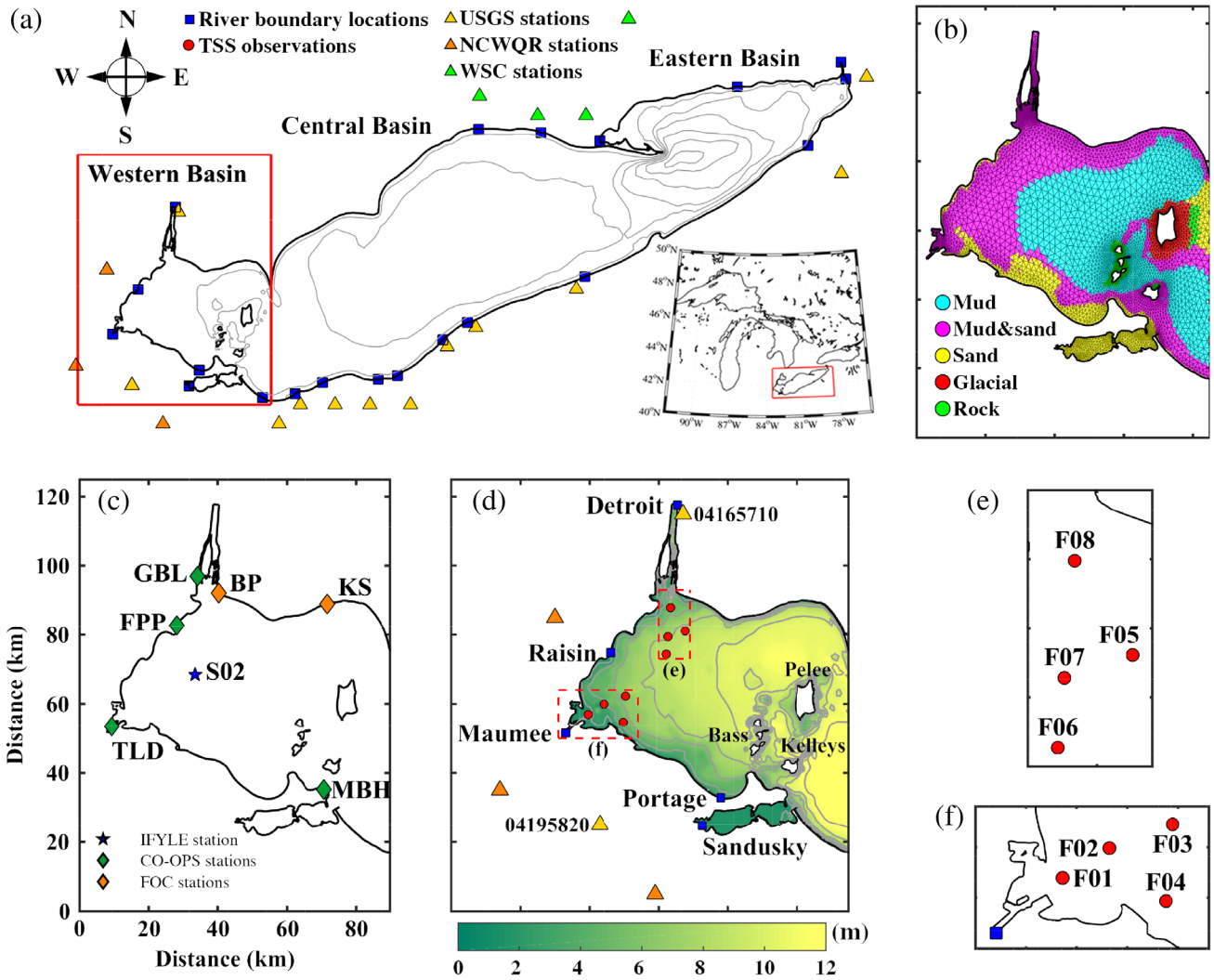

Fig. 2. (**a**) Geometry of Lake Erie and its location among the Laurentian Great lakes; (**b**) model grids and the surficial bed type in the western basin; (**c**) observational hydrodynamic data locations; (**d**) geometry and observational stations in the western basin; and (**e**, **f**): enlarged maps of (**d**) near the Detroit and Maumee River mouths, respectively. Squares: river boundary locations; triangles: river input observations from United States Geological Survey (USGS), National Center for Water Quality Research (NCWQR), and Water Survey of Canada (WSC); blue pentangle: mooring station from International Field Year of Lake Erie (IFYLE), Great Lakes Environmental Research Lab (GLERL), National Oceanic and Atmospheric Administration (NOAA); green diamonds: water elevation gauges from Center for Operational Oceanographic Products and Services (CO-OPS), National Ocean Service (NOS), NOAA; orange diamonds: water elevation gauges from Fisheries and Ocean Canada (FOC); and red circles: observational TSS at 2 m from surface, 2006–2008.

Table 2. Annual sediment loading (m_i in million tonnes per year) and river discharge (F_i in $m^3\ s^{-1}$) into the western basin, 2002–2012, with their contributions to the lake's total loading/discharge. Data source and the sediment concentration (C_i in mg L^{-1}) of each river applied in the model are also presented.

River	m_i	F_i	Data source	Flow-based regression
Detroit	1.3 (5.7%)	5031 (91.9%)	USGS	C_{DE}=1 mg L^{-1}
Maumee	10 (45.4%)	151 (2.9%)	NCWQR	C_{MA}=monitored conc.
Sandusky	2.5 (11.0%)	33 (0.6%)	NCWQR	C_{SD}=monitored conc.
Raisin	0.3 (1.3%)	21 (0.4%)	NCWQR	C_{RS}=monitored conc.
Portage	0.5 (2.1%)	10 (0.2%)	USGS	C_{PT}=2.334 F_{PT} + 15.25

NCWQR, National Center for Water Quality Research; USGS, United States Geological Survey.

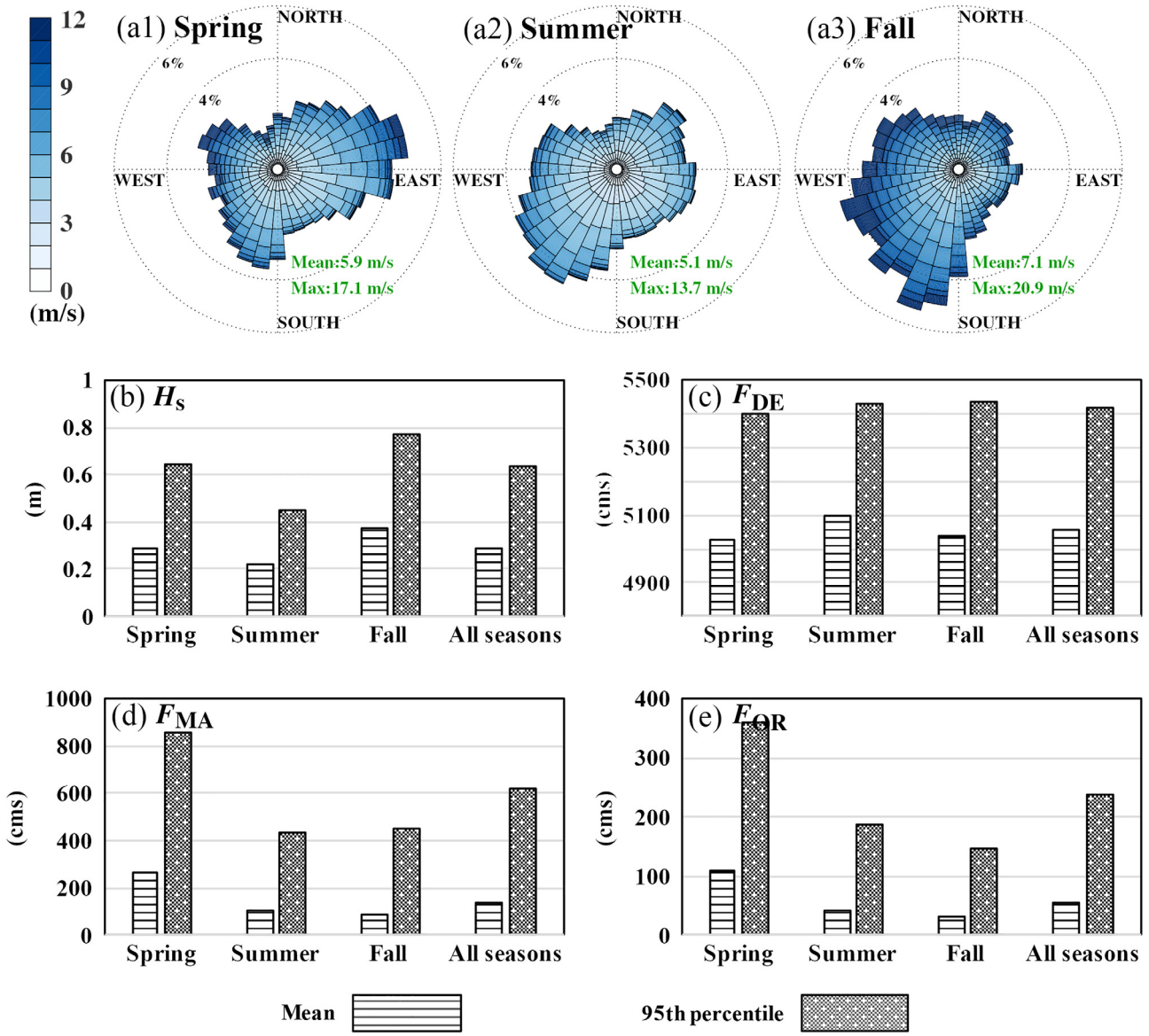

Fig. 3. (**a**) Wind rose diagrams and seasonal variations in the mean and 95th percentile of (**b**) the significant wave heights (H_s), (**c**) the Detroit River discharge (F_{DE}), (**d**) the Maumee River discharge (F_{MA}), and (**e**) and the discharges (F_{OR}) from other rivers (Sandusky, Raisin, and Portage rivers) surrounding the western basin during spring, summer and fall, 2002–2012.

advect and diffuse suspended sediments as Eq. 1; and (2) waves and currents collectively induce the bottom stress that initiates sediment resuspension.

The FVCOM-based wave-current forced sediment model was initially developed and applied in Ge et al. (2015), and the processes incorporated in this study are summarized in Fig. 1b. The hydrodynamic and sediment models were run concurrently, with the system being forced by the hourly wave characteristics from Niu and Xia (2016). Initially, wave characteristics were read into the wave model, where the radiation stress was calculated and passed to the hydrodynamic model that started after it. Afterward, circulations, water elevations, and turbulences from the hydrodynamic model were passed to the sediment model to solve Eq. 1. Then, results from all three models were sent to the BBL model to compute the bottom stress, which was applied in the hydrodynamic model to solve momentum equations and in the sediment model to initiate resuspensions.

Model configurations

Model grids and boundary conditions

The wave-current forced sediment model applied consistent model grids and boundary conditions with the wave-current coupled modeling system in Lake Erie (Niu and Xia 2017).

The model domain covers the entirety of Lake Erie, with a resolution of 0.02–7.7 km in the western basin. Higher resolution grids were assigned in the nearshore areas, and the applied triangle mesh delineates channels of Detroit and Maumee rivers, which are essential for producing river-induced circulations (Niu et al. 2015; Lai et al. 2016). The model applied 20 uniformly distributed sigma layers, giving a vertical resolution in the range of 0.05–0.5 m in the western basin.

Twenty major rivers around Lake Erie, including five surrounding the western basin, were incorporated in the model as open or river boundaries (Fig. 2a). Among them, the Niagara River is the lake's major outlet (5700 $m^3\ s^{-1}$) and was considered as an open boundary (forced with hourly water elevation), whereas the other 19 rivers are inflows and were taken as flow boundaries (forced with daily river discharge and water temperature). Identical to previous model applications (Niu et al. 2015; Niu and Xia 2016, 2017), the model used herein was forced by hourly wind speed at 10 m above ground, air temperature, net downward shortwave radiation, upward long-wave radiation, cloud cover, and relative humidity at the surface. The heat flux was calculated internally by COARE (Coupled Ocean Atmosphere Response Experiment) version 2.6 bulk algorithm.

Configurations of the sediment model in Western Lake Erie

FVCOM-SED in the western basin was configured regarding the classifications of suspended sediment, river loadings, bed properties, and settling velocity calculations. First, suspended sediments were classified into four classes according to their origin: the Detroit River, the Maumee River, the other river inflows (Sandusky, Raisin, and Portage rivers), and resuspension. All sediments were considered as cohesive with a density of 2650 kg m^{-3} and a median size of 4 μm, which conforms to the vastly deposited and suspended grain sizes in the lake (Fukuda and Lick 1980; Hawley and Eadie 2007).

Sediment concentrations and discharges in the Maumee, Sandusky, and Raisin River inflows applied the observations from the National Center for Water Quality Research (NCWQR) at Heidelberg College (orange triangles in Fig. 2d). The Detroit and Portage river discharges were obtained from USGS Sta. 04165710 and Sta. 04195820 (yellow triangles in Fig. 2d), respectively. Missing sediment concentration data from the Portage River discharge were estimated using a linear regression between 2130 observed daily river discharges and sediment concentrations at USGS Sta. 04195820, during 1950–1956 (Table 2). In the absence of observational Detroit River sediment concentrations, a constant of 1 mg L^{-1} was applied, which was determined from monthly mean satellite observations at its river mouth (Binding et al. 2012).

One bed layer with an initial thickness of 0.1 m was applied. This layer had a thin surface layer that is available for erosion. Its thickness is generally at O (10^{-3} m) and was calculated as a function of the maximum instantaneous bottom stress by representative waves and currents. Sediments found on the surficial bed layer of the western basin are nonhomogeneous, and the layer was classified into five types (mud, mud with sand, sand, glacial, and rock) based on the mapping of Thomas et al. (1976) (Fig. 2b). Entrainment properties of each bed type, including the erosion rate constant and the critical shear stresses for erosion and deposition, were specified based on uncertainty tests referring previous observations, laboratory experiments, and parameterizations in other sediment models, which were mainly conducted in Lake Erie and other Great Lakes basins (Table 3).

The model calculated w_s (in mm s^{-1}) as a function of the in situ sediment concentration (C in mg L^{-1}) based on Mehta (1986). Because the basin's maximum sediment concentration stayed below the critical value ($C_{cr} = 10^3$ mg L^{-1}), Eq. 2.2 was not used during the study period. In Eq. 2.1, the Mehta proportional (K_1) and exponential (m) constants were set as 10^{-4} mm s^{-1} and 1, respectively.

$$w_s = \begin{cases} K_1 \cdot C^m \ (C_i < C_{cr}) & (2.1) \\ K_2 \cdot C_{cr}^{m1} [1 - K_3 (C - C_{cr})]^{m2} \ (C_i \geq C_{cr}) & (2.2) \end{cases}$$

The wave-current forced sediment model was applied to produce sediment dynamics in Lake Erie during ice-free cycles (April–November), 2002–2012. The model was initialized on 1st March of each year, with a motionless status and a uniformly distributed thermal structure of 3°C, and a spin-off of 1 month. The simulations ended on 30th November 2002 to 2012. The internal mode (baroclinic) time step of the modeling system integration was 8 s, with that of the external mode (barotropic) being 2 s.

Observational data and model evaluations

The model's ability to produce hydrodynamics, wave dynamics, and suspended sediments in Western Lake Erie was evaluated by comparing the model results with field observed water elevations, current velocities, wave characteristics, and total suspended sediment concentrations (TSS). Hourly surface-water elevations during 2002–2012 at four stations along the U.S. coastline (green diamonds in Fig. 2c) were obtained from the Center for Operational Oceanographic Products and Services (CO-OPS), National Ocean Service (NOS), National Oceanic and Atmospheric Administration (NOAA), whereas those from two stations along the Canadian coastline (orange diamonds in Fig. 2c) were obtained from Fisheries and Ocean Canada (FOC). Current velocities, significant wave height, and peak wave period were compared with field data at one mooring station of S02 (in situ water depth of 8 m) during 2005 (Fig. 2c). These data were acquired from the physical dataset of IFYLE (International Field Year of Lake Erie), managed by the Great Lakes Environmental Research Laboratory (GLERL), NOAA.

TSS were collected at 2 m from the water surface at eight stations surrounding the Maumee and Detroit River mouths during May–July 2006–2008 (locations noted in Fig. 2d–f). In addition,

Table 3. Entrainment properties for different sediment types on the surficial bed layer applied in the western basin, including the erosion rate constant (E) and the bottom critical stresses for erosion (τ_{ce}) and deposition (τ_{cd}).

	E (kg m^{-2} s^{-1})		τ_{ce} (N m^{-2})		τ_{cd} (N m^{-2})	
Bed type	**Applied**	**Reference**	**Applied**	**Reference**	**Applied**	**Reference**
Mud	3.6×10^{-6}	10^{-7}–10^{-3} (1, 2)	0.05	0.03–0.3 (1, 3–10)	0.1	0.04–0.16 (5, 9)
Mud with sand	3.5×10^{-6}		0.06			
Sand	3.4×10^{-6}		0.07	0.9–1.92 (6, 8)		
Glacial sediments	1×10^{-7}		2			
Bedrock	1×10^{-8}		5			

(1) Fukuda and Lick (1980); (2) Lee et al. (1981); (3) Lick et al. (1994); (4) Lou et al. (2000); (5) Cardenas et al. (2005); (6) Hawley and Eadie (2007); (7) Harris et al. (2008); (8) Hawley et al. (2009); (9) Morales-Marin et al. (2017); and (10) Valipour et al. (2017).

the sediment model's skill was qualitatively validated with true-color images from the Moderate Resolution Imaging Spectroradiometer (MODIS) on the National Aeronautics and Space Administration (NASA) satellites Aqua and Terra. The images were obtained from the Space Science and Engineering Center (SSEC) at the University of Wisconsin-Madison.

Model performance was assessed using the Pearson correlation coefficient (r), the root-mean-square deviation (RMSD), the percentage bias (P_{bias}) between two scalars x (model simulation) and y (observation), where n is the total number of observations, and $\overline{x}$ and $\overline{y}$ are the means of x and y, respectively.

$$R=\frac{\sum_{i=1}^{n}(x_i-\overline{x})(y_i-\overline{y})}{\sqrt{\frac{1}{n}\sum_{i=1}^{n}(x_i-\overline{x})^2}\sqrt{\frac{1}{n}\sum_{i=1}^{n}(y_i-\overline{y})^2}}$$

$$\mathrm{RMSD}=\sqrt{\frac{\sum_{i=1}^{n}(x_i-y_i)^2}{n}}$$

$$P_{\mathrm{bias}}=\frac{\overline{x}-\overline{y}}{\overline{y}}$$

In addition, the vector correlation coefficient (VR) between two vectors $\vec{v_1}=u_1\vec{i}+v_1\vec{j}$ and $\vec{v_2}=u_2\vec{i}+v_2\vec{j}$ were calculated to evaluate the model's skill in producing current velocities.

$$\mathrm{VR}^2=\mathrm{TR}\left(\left(\sum 11\right)^{-1}\sum 12\left(\sum 22\right)^{-1}\sum 21\right)$$

In the definition of VR, $\sum ij=\begin{bmatrix}\sigma(u_i,u_j) & \sigma(u_i,v_j)\\ \sigma(v_i,u_j) & \sigma(v_i,v_j)\end{bmatrix}$, σ is the correlation covariance, and TR is the trace of the products of the $\sum ij$ submatrices.

Study periods and terminology

As external forcing overlying the western basin has distinctive seasonal variations (Fig. 3), the sediment dynamics were studied during spring (April–May), summer (June–August), and fall (October–November) during 2002–2012. In addition to looking at seasonal patterns, relative contributions of river-loaded vs. resuspended sediments to HTEs were evaluated during the Maumee River floods (Maumee River discharge, i.e., F_{MA} > 500 m^3 s^{-1}; in total of 33 floods during the study period). Among them, two 9-d late-spring flood events (one in 2003 and the other in 2011) were exanimated thoroughly. These events occurred when F_{MA} exceeded the 99th percentile value (1099 m^3 s^{-1}) during the 11-yr study period. In particular, the flood of 2003 (hereafter flood03) had a peak Detroit River discharge (F_{DE}) and F_{MA} of 5171 m^3 s^{-1} and 1766 m^3 s^{-1}, respectively, and was accompanied by strong wind and waves (Fig. 4a1–e1). The flood of 2011 (hereafter flood11) had a higher peak F_{DE} and F_{MA} (5513 m^3 s^{-1} and 2217 m^3 s^{-1}, respectively) but was forced by more relaxed wind and waves (Fig. 4a2–e2).

Surface sediment concentration (SSC) refers to the mean sediment concentration of the surface 1-m layer. HTEs were recognized as when and where SSC exceeded 30 mg L^{-1}. HTEs with an affected area that covered more than one third of the basin (~ 1000 km^2) were recognized as the basin-wide HTEs. The HTEs durations were defined as the integrated periods when HTEs appeared. Meanwhile, regions with sediments from the Maumee River, the other rivers, or resuspension contributed more than 50% to in situ SSC in high-turbidity patches were identified as the respective dominancy. Areas with both river loading and resuspension contributed more than 30% to in situ SSC in high-turbidity patches were recognized as the collective dominancy.

Validation of the wave-current forced sediment model in Western Lake Erie

Validation of the wave-current coupled modeling system in Western Lake Erie

The wave-current coupled modeling system has satisfactory skills in producing hydrodynamics and wave dynamics in Lake Erie (Niu et al. 2015; Niu and Xia 2016, 2017). However, as small errors in the wave and/or hydrodynamic models could be amplified in the sediment model owning to the power-dependence of the sediment transport rates on the flow velocities (Amoudry and Souza 2011), the system's ability to simulate

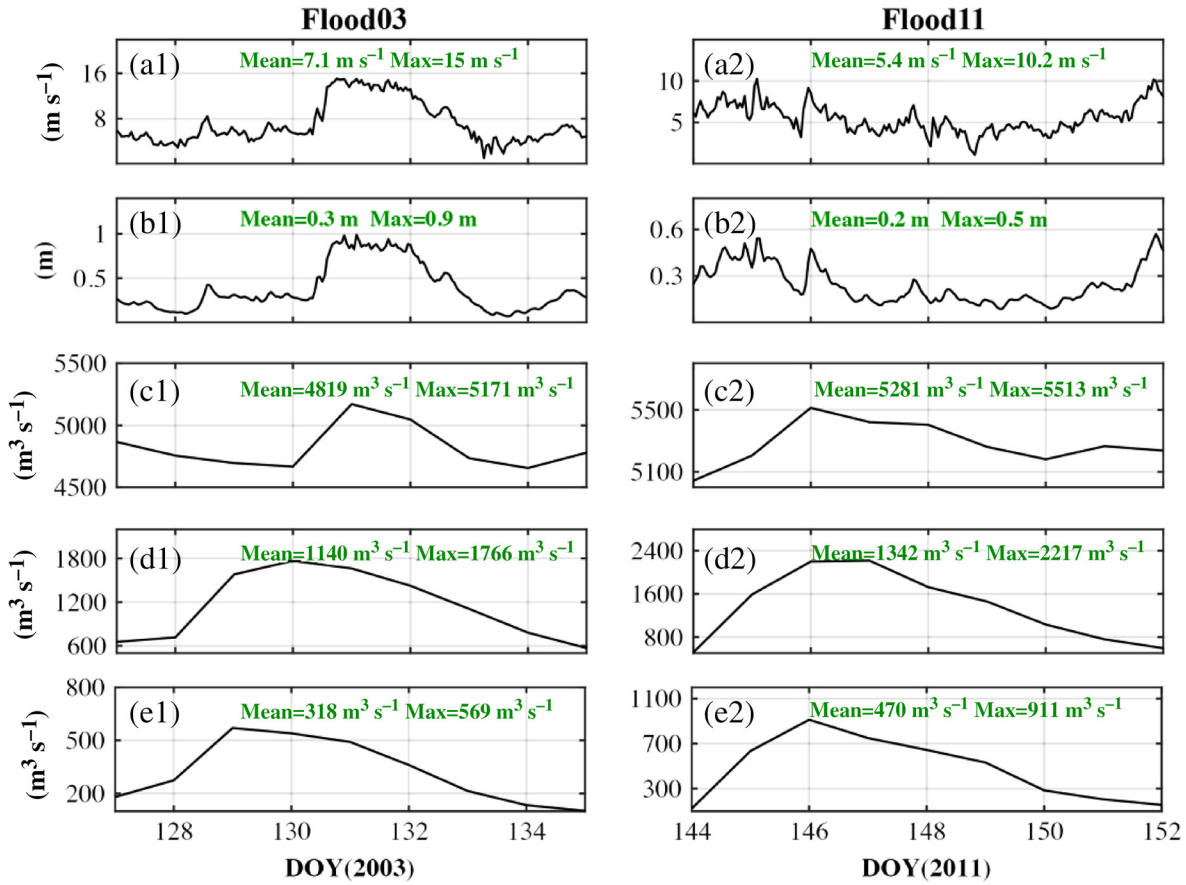

Fig. 4. Time-series of (**a**) wind speed, (**b**) significant wave height, (**c**) Detroit River discharge, (**d**) Maumee River discharge, and (**e**) river discharge from Raisin, Sandusky, and Portage rivers in the western basin during flood03 (2003-05-08 to 2003-05-16) and flood11 (2011-05-25 to 2011-06-02).

the physical processes in the western basin was further validated before its application to drive the sediment model.

Modeled water elevations were compared with observations at six gauges surrounding the western basin (locations noted in Fig. 2c) during 2002–2012. Results indicate that the wave-current modeling system has satisfactory skills in producing the observed water elevations, with r values ranged 0.74–0.92; and RMSDs ranged 0.04–0.14 m (Table 4). In addition, the system reasonably simulated the observed current velocities at S02 during 2005 (Table 5), with a vector correlation coefficient of 0.74 and RMSD of 0.03 m s^{-1} in producing both the eastward and northward current velocities. The simulated wave characteristics (significant wave height and peak wave period, i.e., H_s and T_p) are consistent with the observations at S02 (Table 5). The model-simulated and observed H_s have a r of 0.81, RMSD of 0.14 m, and percentage bias (P_{bias}) of 9.9%, respectively. The model-simulated and observed T_p have a r of 0.43, RMSD of 0.56 s, and P_{bias} of –8.3%, respectively.

In general, the wave-current coupled modeling system has satisfactory skills in producing hydrodynamics and wave dynamics in the western basin of Lake Erie. The system has been successfully applied in driving an ecological model in Western Lake Erie (Jiang et al. 2015), and it sets a solid basis for the sediment model.

Validation of the sediment model in Western Lake Erie

To validate the wave-current forced sediment model in Western Lake Erie, model results were compared with 77 observed TSS at eight stations (Fig. 2d–f) near the Detroit and Maumee River mouths during May–July 2006–2008. Meanwhile, simulated SSC patterns were compared with corresponding MODIS true-color images to assess the model's skill in capturing the spatial and temporal variations of HTEs in the basin.

As the model applied a constant sediment concentration (1 mg L^{-1}) in the Detroit River discharge, it showed less satisfactory concordance with the observed TSS near the Detroit River mouth (Fig. 5e–h; r = –0.07, p = 0.66; RMSD = 5.1 mg L^{-1}). The discrepancies could result from the model's exclusion of the occasional turbid Detroit River discharge induced by the resuspension in Lake St. Clair. On the other hand, the model could reasonably produce the observed TSS near the Maumee River mouth (Fig. 5a–d; r = 0.77, p < 0.01; RMSD = 28.2 mg L^{-1}). Albeit the relatively large RMSD, the model captured the TSS variation trend at each station, as well as the conspicuous spatial differences among the stations (decreasing TSS from F01 to F04). The errors mainly resulted from the model's failure in producing high TSS at F01 (located inside the Maumee Bay; Fig. 5a). By

Table 4. Pearson correlation coefficient (*r*) and RMSDs between the model-simulated and observed water elevations at six stations in the western basin of Lake Erie during 2002–2012.

		TLD	FPP	GBL	BP	KS	MBH
r (%)	2002	85.95	89.2	77.71	86.09	82.70	84.72
	2003	87.93	89.24	82.57	87.75	85.19	85.83
	2004	88.69	88.99	80.40	86.34	81.66	84.90
	2005	91.05	90.40	82.08	87.49	85.06	88.69
	2006	90.64	89.78	80.06	87.92	82.91	85.05
	2007	91.02	90.87	82.8	88.08	84.33	84.87
	2008	89.49	88.5	74.76	85.11	81.98	84.16
	2009	92.43	90.9	78.34	87.8	82.11	84.99
	2010	91.5	89.61	76.17	87.06	78.54	83.22
	2011	89.92	87.63	81.36	81.69	78.2	83.24
	2012	87.97	86.36	81.7	83.49	77.1	81.8
RMSD	2002	0.1	0.07	0.14	0.07	0.06	0.05
(m)	2003	0.09	0.06	0.12	0.06	0.05	0.05
	2004	0.09	0.06	0.12	0.06	0.05	0.05
	2005	0.09	0.07	0.12	0.07	0.06	0.05
	2006	0.08	0.06	0.13	0.07	0.06	0.05
	2007	0.07	0.05	0.11	0.05	0.04	0.04
	2008	0.06	0.05	0.09	0.05	0.04	0.04
	2009	0.06	0.05	0.11	0.06	0.05	0.04
	2010	0.07	0.05	0.12	0.06	0.05	0.05
	2011	0.07	0.06	0.09	0.06	0.05	0.05
	2012	0.07	0.05	0.1	0.06	0.05	0.05

contrast, those in the basin (Sta. F02 to F04) were better simulated (Fig. 5b–d; $r = 0.78$, $p < 0.01$; RMSD = 16.5 mg L^{-1}).

The model-simulated SSC were compared with available cloud-free MODIS true-color images during 402 episodes in 2003–2012, and results during 12 representative episodes were presented in Fig. 6. The comparisons demonstrated that themodel well simulated the characteristic SSC patterns in Western Lake Erie. For example, the basin remained clear under weak wind ($U_{wnd} < 5$ m s^{-1}) and low river discharge conditions ($F_{MA} < 200$ m^3 s^{-1}; Fig. 6a). During floods ($F_{MA} >$ 500 m^3 s^{-1}) forced by weak wind, high SSC appeared and concentrated near the river mouths (Fig. 6b), which conforms to the coastal river plume patterns under weak wind forcing (e.g., Xia et al. 2011; Jiang and Xia 2016). When there was strong wind ($U_{wnd} > 8$ m s^{-1}) overlying the basin's surface, the majority of the basin was turbid. High SSC concentrated in the southern basin and near the islands, where the lake's bottom was more subjective to the wave's orbital velocities (Niu and Xia 2016). Meanwhile, clear water from the Detroit River and central basin diluted SSC along the northern shore and eastern coast, respectively (Fig. 6c).

Overall, while uncertainties still exist in producing sediment dynamics in Western Lake Erie with the wave-current forced sediment model, the model reasonably captured the spatial and temporal variations of the basin's HTEs, making it a valid tool for this study's objectives.

Table 5. Pearson correlation coefficient (*r*), vector correlation coefficient (VR), RMSDs and percentage bias (P_{bias}) between the model-simulated and observed current velocities (*u*: eastward; *v*: northward), significant wave heights (H_s), and peak wave periods (T_p) at S02 during 2005.

		r (%)	RMSD	P_{bias}	VR (%)
Current velocity	*U*	64.89	0.03 m s^{-1}	—	73.56
	V	32.04	0.03 m s^{-1}	—	
	H_s	80.77	0.14 m	9.85	—
	T_p	43.26	0.56 s	–8.26	—

Results and discussions

Using the calibrated and validated wave-current forced sediment model, driving factors of the suspended sediment plumes were investigated. Afterward, seasonal variations in the SSCs and HTEs were given assessment. Then, relative contributions of river loading vs. resuspension to HTEs were discussed on the seasonal scale, as well as during flood events.

Driving factors of the suspended sediments in the Western basin of Lake Erie

Impacts of wind speed (U_{wnd}), significant wave height (H_s), Detroit River discharge (F_{DE}), and Maumee River discharge (F_{MA}) on the basin's hourly and monthly mean SSCs in Western Lake Erie were analyzed. Results showed that wind and waves played dominant roles in initiating high SSCs in the entirety of the western basin, especially on the monthly mean scale ($r > 0.8$ in ~ 70% of the basin; Fig. 7b1,b2). The finding is consistent with previous researches in similar shallow-water environments (e.g., Hawley and Eadie 2007; Green and Coco 2014; Valipour et al. 2017). On an hourly temporal scale, wind and waves had a large effect on SSCs in the southern part of the basin ($r > 0.3$) and were less important near the Detroit River mouth and along the eastern part of the basin (Fig. 7a1, a2), where SSC were influenced by the dilution from the Detroit River inflows and central basin intrusions. Meanwhile, F_{DE} had nearly no impact on the hourly SSC (Fig. 7a3) and was negatively ($r < -0.2$) related to the monthly mean SSC in the southern part of the basin (Fig. 7b3), as it carried low-SSC water from the upper Great Lakes and accelerated the eastward transport from the western to the central basin (Niu et al. 2015). By contrast, F_{MA} dominated SSC at the Maumee River mouth ($r > 0.5$) on both the hourly and monthly mean temporal scale. The impacts of F_{MA} were confined to the southwest and causing prominent nearshore to offshore gradients (Fig. 7a4,b4).

In general, the Western Lake Erie's sediment dynamics appear to be collectively driven by wind waves and river

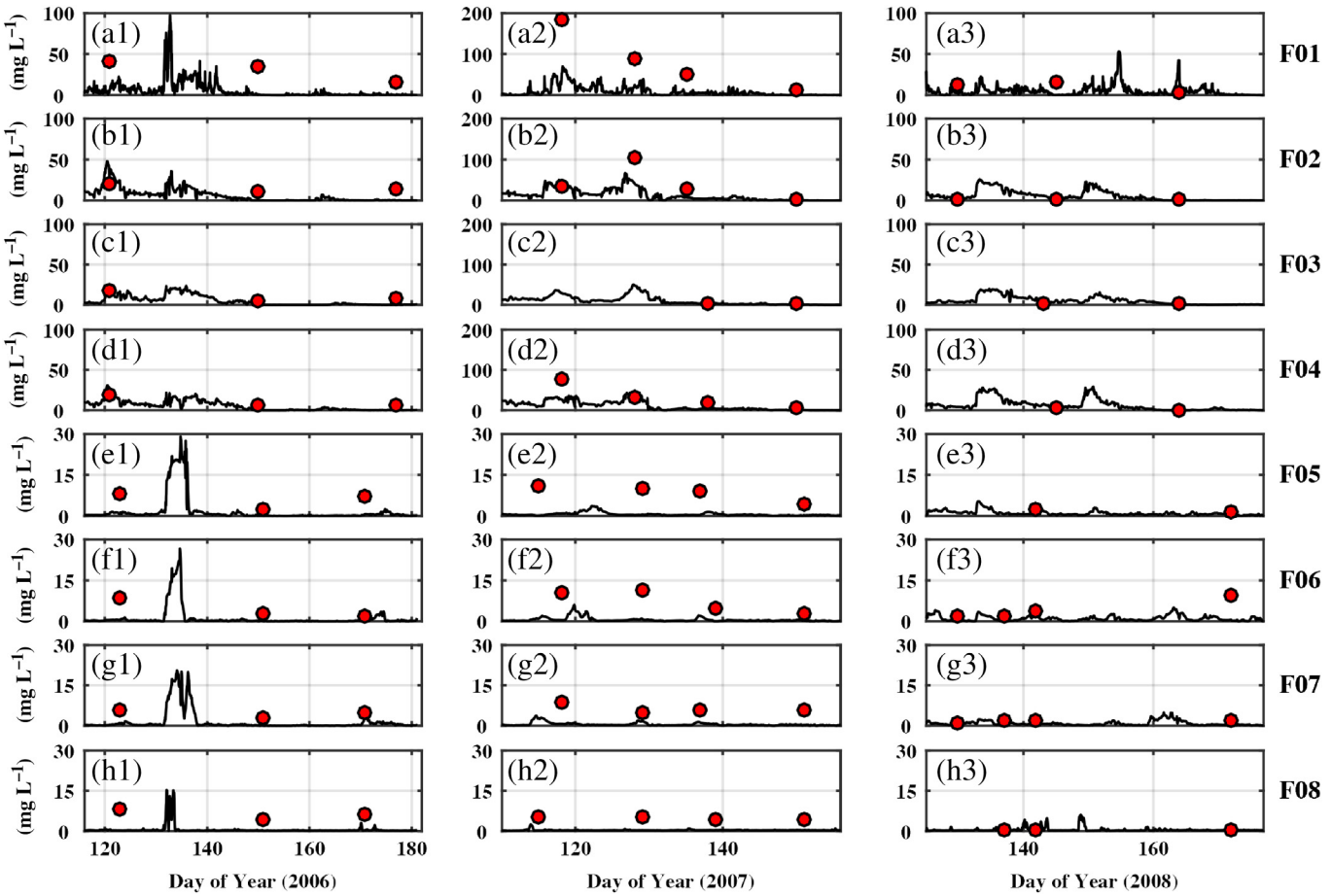

Fig. 5. Observed (red circles) vs. simulated (black lines) TSS from 2 m below the water surface at stations near the Maumee (**a**–**d**) and Detroit (**e**–**h**) River mouths, 2006–2008.

discharges, the dominancy of which had distinctive spatial variations. Given that variations in the main driving factors (Fig. 3) induced prominent seasonality in the basin's hydrodynamics and wave dynamics (Bai et al. 2013; Niu et al. 2015; Niu and Xia 2016), the variations in the basin's mean and extreme suspended sediment dynamics on the seasonal scale were then investigated.

Seasonal variations in SSCs and HTEs in Western Lake Erie

SSCs in the western basin showed substantial seasonality in both its mean values and the seasonal-mean SSC patterns, owing to their domination by both river loading and resuspension. The basin was generally turbid during spring and fall (Fig. 8), with the mean SSC being 10.3 mg L^{-1} and 17.8 mg L^{-1}, respectively. During these two seasons, relatively high SSC (> 15 mg L^{-1}) appeared in the southern portion of the basin (Fig. 8a3,c3), which are related to the strong wind and waves during the two seasons (Fig. 3a,b). During spring, high SSC also exist at the river mouths corresponding to the high river discharges during the season (Fig. 3d,e). In addition, the westward transport of low-turbidity water from the central to the western basin was bounded at the eastern coast due to the hydraulic gradient (Niu et al. 2015). During summer, the basin was clear with a mean SSC of 0.9 mg L^{-1}, and relatively high SSC (> 5 mg L^{-1}) concentrated around the river mouths, particularly in the Maumee and Sandusky bays (Fig. 8b3). These results are in accordance with previous satellite observations (Binding et al. 2012).

In addition to the variations in the seasonal-mean SSC, extreme sediment dynamics (i.e., HTEs) in the western basin had prominent seasonality as well. In general, HTEs occurred most frequently during fall and moderately during spring, with higher frequencies (> 15%) in the southern basin and near river mouths (Fig. 8a4,c4). During summer, HTEs seldom occurred in offshore areas of the western basin, with those that did occur being located near the river mouths (Fig. 8b4). Meanwhile, Fig. 9 indicated that the HTEs had relatively broader influenced areas during spring (mean and 95th percentile of 91 km^2 and 589 km^2) and fall (222 km^2 and 1174 km^2), with longer durations (mean of 3.2 d and 4.4 d during spring and fall, respectively). On the contrary, HTEs during summer (Fig. 9b) often had a limited influenced area (mean and 95th

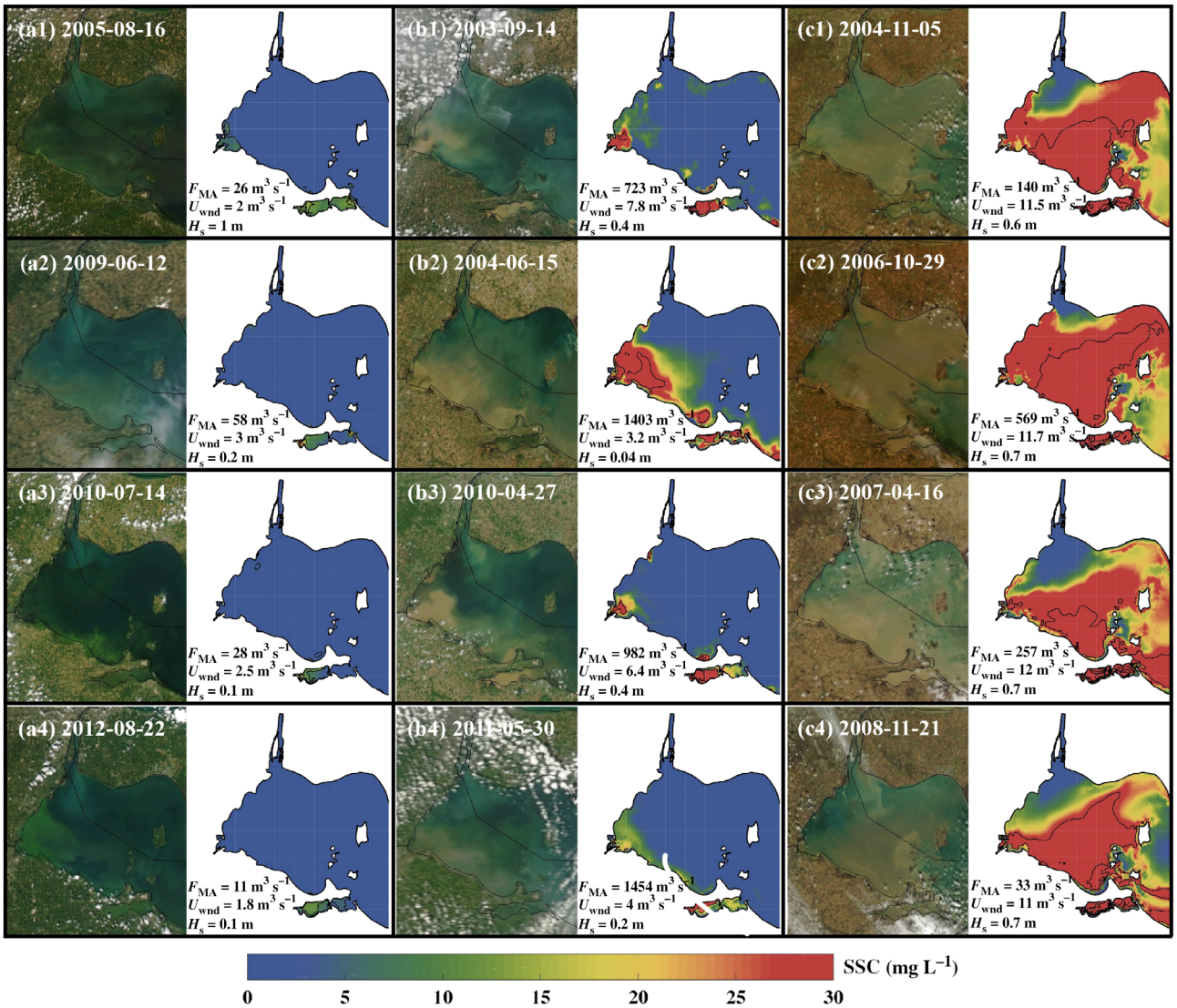

Fig. 6. Comparisons between the MODIS true-color satellite images and model-simulated SSCs in Western Lake Erie during the episodes when the western basin has (**a**) a basin-wide clear state; (**b**) high-turbidity patches near the river mouths; and (**c**) a basin-wide turbid state, with corresponding Maumee River discharge (F_{MA}), wind speed (U_{wnd}) and significant wave height (H_s).

percentile of 21 km^2 and 57 km^2) and were less persistent (mean duration of 1.5 d). In addition, basin-wide HTEs (HTE size > 1000 km^2) occurred most frequently during fall (27.4%), occasional during spring (8.1%), and never appeared during summer in our study period (Fig. 9).

Relative contributions of river loading vs. resuspension to HTEs in Western Lake Erie

The drivers of HTEs varied seasonally. The durations and influenced areas of river-induced HTEs were comparable during spring (Fig. 9a) and summer (Fig. 9b), but they were negligible during fall (Fig. 9c). Unlike river-induced HTEs, resuspension-induced HTEs were most prominent during fall (Fig. 9c), moderate during spring (Fig. 9a), and negligible during summer (Fig. 9b). Accordingly, the spring and fall HTEs were mainly (> 85%) induced by resuspension, whereas contributions of river loading were confined to areas near the river mouths during spring (Fig. 8a5) and were negligible during fall (Fig. 8c5). During summer, the occasionally appeared HTEs were largely (~ 90%) generated by river inputs, except for those along the northern and southern shorelines that originated from resuspension (Fig. 8b5). Meanwhile, the river loading and resuspension had distinctive spatial dominances in HTE generations; the collectively induced HTEs rarely occurred during any of the seasons (< 0.1%).

Extended investigations showed that the resuspension-induced HTEs had a broader area of influence (mean and 95th percentile of 105 km^2 and 602 km^2) and existed for a longer

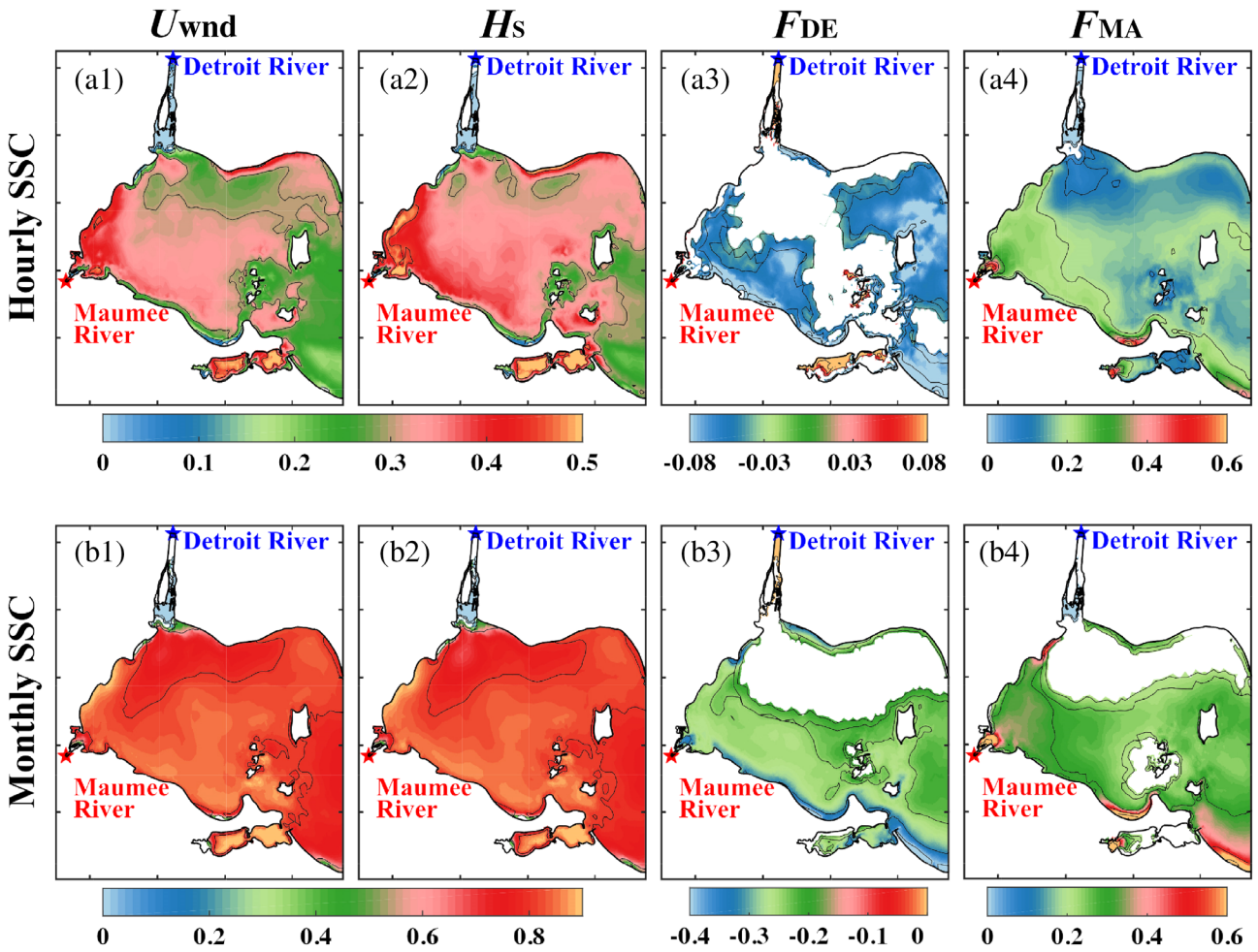

Fig. 7. Pearson correlation coefficients (r; $p < 0.05$) between the (**a**) hourly and (**b**) monthly mean SSCs and external forcings, including the basin-averaged wind speed (U_{wnd}) and significant wave height (H_s), Detroit River discharge (F_{DE}) and Maumee River discharge (F_{MA}) from 2002 to 2012 in Western Lake Erie.

duration than river-driven HTEs (mean and 95th percentile of 2.3 d and 11.3 d; Fig. 9d). These are at the same order of magnitude with previous observations in other areas within the Great Lakes basins (e.g., Lou et al. 2000; Hawley and Eadie 2007; Valipour et al. 2017). While river-induced HTEs had limited impact areas (mean and 95th percentile of 14 km^2 and 44 km^2), and they lasted for a short period of time (mean and 95th percentile of 0.8 d and 4 d) with pulsing river discharges.

Although the above investigations illustrated the dominancy of resuspension over river loading in HTE formations, whether the result is consistent during heavy runoff events remained unclear. Therefore, HTE origins were further investigated during the two selected floods (flood03 and flood11). Between them, flood03 had high river discharges accompanied with strong wind waves (Fig. 4). During the flood, river-induced high SSC were confined near the river mouths (Fig. 10a1), generating small HTE patches (mean and maximum of 46 km^2 and 141 km^2, respectively) throughout flood03 (~ 9 d) in the Maumee and Sandusky bays (Figs. 10a4, 11a). After day 131 of 2003, wind and waves started growing stronger (Fig. 4a1,b1). Subsequently, intense wave-current induced bottom stress (τ_{cw}) initiated strong resuspensions throughout the basin, which quickly predominated over the river-induced HTE in 3 h (Fig. 11a). During the remaining flood03, the resuspension-induced HTE had an influenced area with a mean and maximum of 940 km^2 and 2394 km^2, and played dominant roles in majority of the basin (Fig. 10a5).

Unlike flood03, flood11 was driven by weak wind waves and high-river discharges (Fig. 4). Subsequently, turbid patches appeared near the river mouths (Fig. 10b3) were induced mainly by river loading (Fig. 10b1). Meanwhile, resuspension contributed ~ 5 mg L^{-1} SSC near the Maumee River mouth (Fig. 10b2), resulting from the corresponding high τ_{cw} (8.9×10^{-5} Pa) generated by the rapid F_{MA}-induced currents ($\tau_c = 7.5 \times 10^{-5}$ Pa), which is typical in wave-sheltered channel systems (e.g., Wang et al. 2014). As a result, HTE concentrated near the river mouths throughout

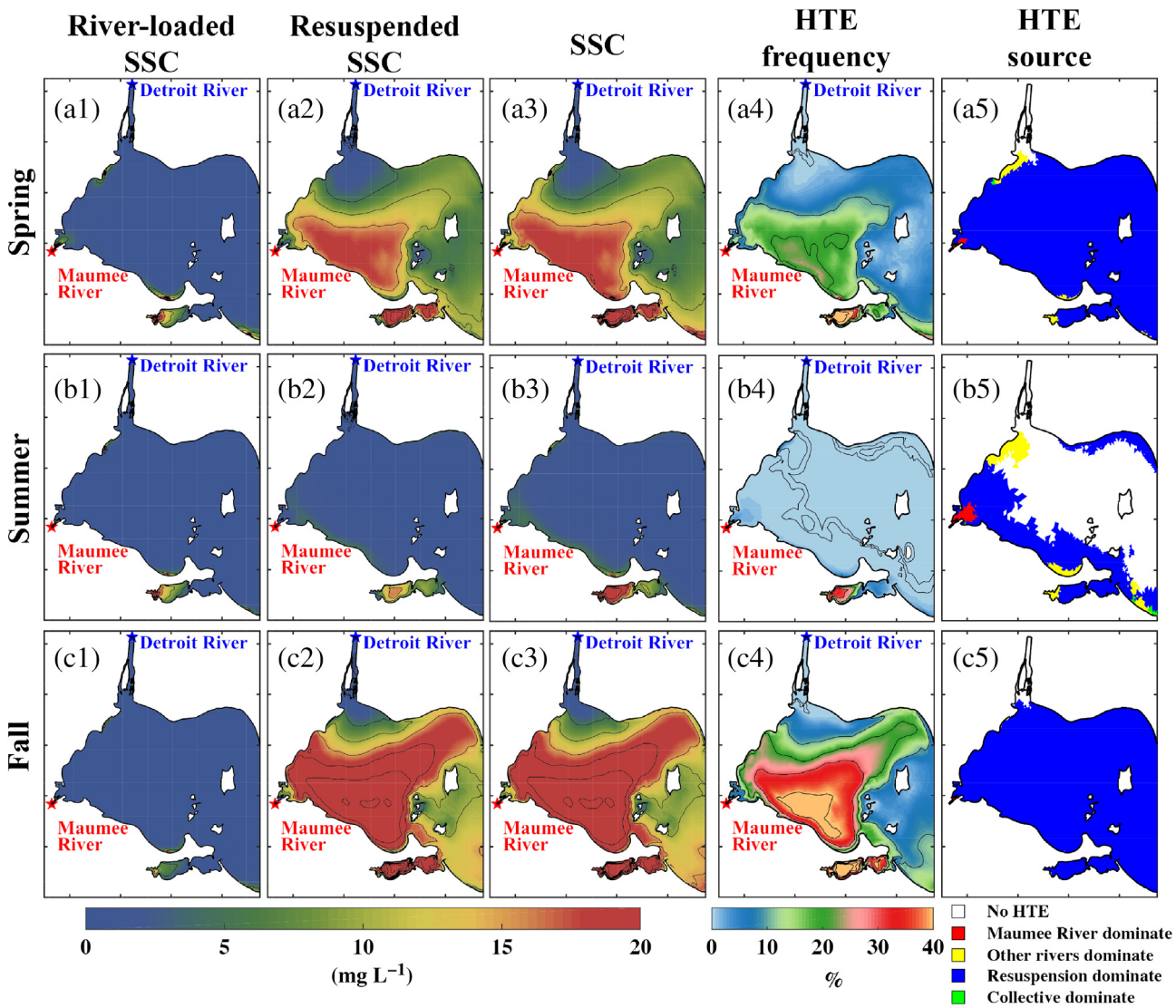

Fig. 8. Seasonal-mean river-loaded, resuspended and overall SSCs, as well as the frequency and origins of HTEs in Western Lake Erie during (**a**) spring, (**b**) summer, and (**c**) fall, 2002–2012.

flood11 and originated from rivers in the main (Figs. 10b5, 11b). Nevertheless, the area of the river-induced HTE patch was still limited (mean and maximum of 79 km^2 and 152 km^2; Fig. 11b), and its impacts hardly penetrated into the offshore regions (Fig. 10b).

Although the predominance of river loading over resuspension in generating HTEs (e.g., flood11) rarely (< 1%) happened during the 11 model simulation years, they are typical (> 40%) during floods with $F_{MA} > 500\ m^3\ s^{-1}$ (in total of 33 events during our study period). In general, their contributions to HTEs are non-negligible during floods: if excluding the river-loaded sediment plumes, the HTE patch sizes during the corresponding floods would be reduced by 11.3%. These results are consistent with previous findings in coastal systems under the impacts of estuarine outflow plumes (Garel et al. 2009; Shen et al. 2013).

Conclusions

Our study investigated the relative contributions of river loading vs. resuspension to HTEs in Western Lake Erie during ice-free cycles (April–November) of 2002–2012 using a wave-current forced sediment model. Uncertainties still exist in this model owing to the simplifications of sediment dynamics applied in FVCOM-SED, inaccurate boundary conditions (e.g., bed properties) due to the lack of observations, and inevitable errors in producing the basin's hydrodynamics and wave dynamics. Nevertheless, the model reasonably captured the occurrence and influenced area of HTEs in the basin.

The modeling conducted herein showed that SSCs and HTEs in the basin were dominated by wind and waves in the offshore regions, and were driven by river loadings near the mouths. Meanwhile, low-turbidity water masses from the Detroit River and the central basin were shown to dilute the SSC near the

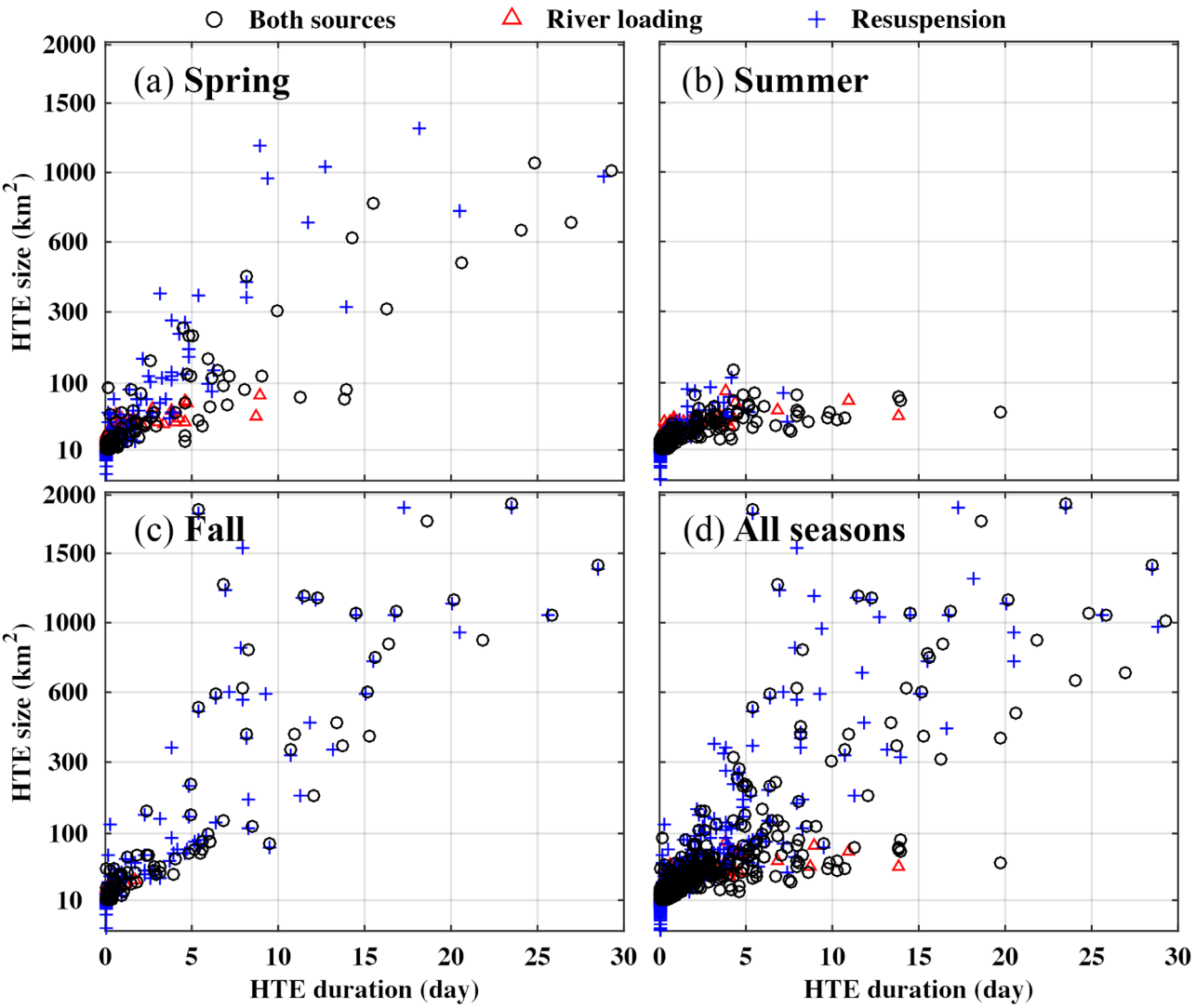

Fig. 9. Duration vs. patch sizes of HTEs that occurred during (**a**) spring, (**b**) summer, (**c**) fall, and (**d**) all seasons in Western Lake Erie, 2002–2012. Black circles: HTE induced by the collective contributions of river loadings and resuspension; red triangles: HTE induced by river loading; blue crosses: HTE induced by resuspension.

northern shore and the eastern boundary, respectively. It is noteworthy that both the Detroit and Maumee River plumes have non-negligible influences on the basin's sediment dynamics. However, the dynamics and interactions between the turbid and eutrophic Maumee River plume and the clear and oligotrophic Detroit River plume under various wind forcing are not the focus of this study and require further investigations. Owing to the seasonally varying wind waves and river discharges, the Western Lake Erie was turbid during spring and fall with frequent (> 15%), broad (mean of 91 km^2 and 222 km^2 during spring and fall, respectively) and persistent (mean of 3.2 d and 4.4 d during spring and fall, respectively) HTEs in the southern basin and near the river mouths. During summer, the basin was clear with occasional (< 1%), small (mean of 21 km^2) and short (mean of 1.5 d) HTEs near the river mouths.

Results demonstrated that river loading and resuspension had distinct spatial dominancy in HTE generations. In general, resuspension-induced HTEs seldom appeared during summer, and they were more prominent during spring and fall. Resuspension generated broad (O [10^2–10^3 km^2]) HTE patches during storms and they were the major contributor to HTEs in the offshore areas. By contrast, river-induced HTEs mainly occurred during spring and summer. They generated relatively smaller (O [1–10^2 km^2]) HTE patches at their river mouths, and they were incapable of generating basin-wide HTEs even during heavy runoff events. Even so, river-loaded sediments are non-negligible in making Western Lake Erie such a turbid ecosystem. Through increased sediment supply, they enlarged the turbid patch size by 11.3% during flood periods.

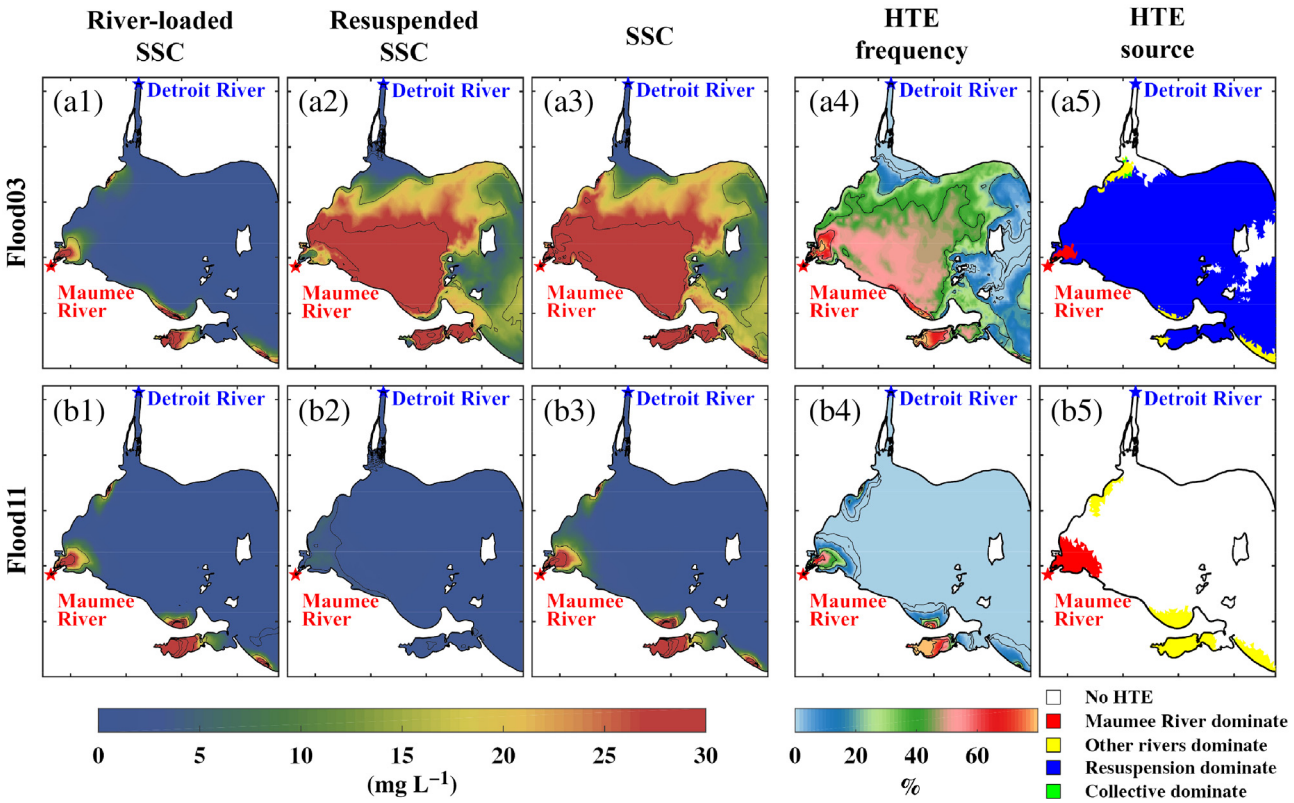

Fig. 10. River-loaded, resuspended and overall SSCs, as well as the frequency and origins of HTEs in Western Lake Erie, during (**a**) flood03 and (**b**) flood11.

Overall, our study demonstrated the dominance of resuspension and the non-negligible contributions of river loading to HTEs in Western Lake Erie and constitutes basis of understanding their relative contribution in similar river-dominated and wave-energetic ecosystems (e.g., lakes, estuaries, and coastal lagoons). The spatial and temporal variations in the dominancy of sediments from different origins highlight the necessity of applying source-specified sediment models in future studies. By providing spatial and temporal varying internal and external sediment and nutrient loadings, better

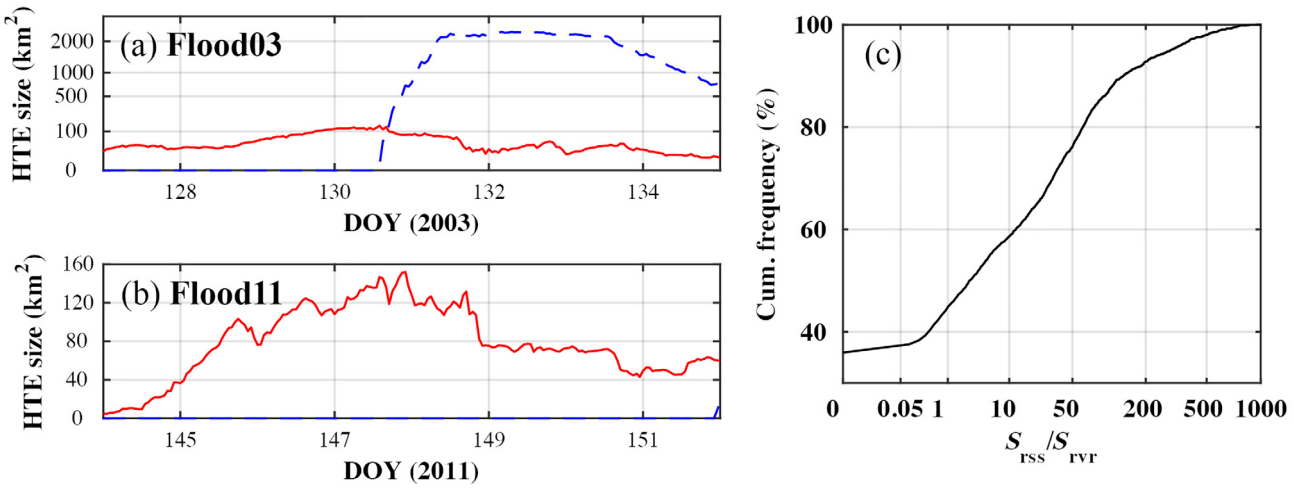

Fig. 11. HTE patch size from river loadings (red solid) and resuspensions (blue dashed) during (**a**) flood03 and (**b**) flood11 in Western Lake Erie. (**c**) Cumulative frequency of the ratio between resuspension induced high-turbidity patch areas (S_{rss}) and those induced by river loadings (S_{rvr}) during Maumee River floods (F_{MA} > 500 m^3 s^{-1}), 2002–2012.

linked physical-biological models could be developed to describe the dynamics of these ecosystems, including the valued biota that they support, both now and in the face of continued human-driven environmental change.

References

Amoudry, L. O., and A. J. Souza. 2011. Impact of sediment-induced stratification and turbulence closures on sediment transport and morphological modelling. Cont. Shelf Res. **31**: 912–928. doi:10.1016/j.csr.2011.02.014

Bai, X., J. Wang, D. J. Schwab, Y. Yang, L. Luo, G. A. Leshkevich, and S. Liu. 2013. Modeling 1993–2008 climatology of seasonal general circulation and thermal structure in the Great Lakes using FVCOM. Ocean Model. **65**: 40–63. doi:10.1016/j.ocemod.2013.02.003

Binding, C. E., T. A. Greenberg, and R. P. Bukata. 2012. An analysis of MODIS-derived algal and mineral turbidity in Lake Erie. J. Great Lakes Res. **38**: 107–116. doi:10.1016/j.jglr.2011.12.003

Bolsenga, S. J., and C. E. Herdendorf. 1993. Lake Erie and Lake St. Clair handbook. Wayne State Univ. Press, p. 467.

Cardenas, M. P., D. J. Schwab, B. J. Eadie, N. Hawley, and B. M. Lesht. 2005. Sediment transport model validation in Lake Michigan. J. Great Lakes Res. **31**: 373–385. doi:10.1016/S0380-1330(05)70269-0

Carey, C. C., and E. Rydin. 2011. Lake trophic status can be determined by the depth distribution of sediment phosphorus. Limnol. Oceanogr. **56**: 2051–2063. doi:10.4319/lo.2011.56.6.2051

Carpenter, S. R., N. F. Caraco, D. L. Correll, R. W. Howarth, A. N. Sharpley, and V. H. Smith. 1998. Nonpoint pollution of surface waters with phosphorus and nitrogen. Ecol. Appl. **8**: 559–568. doi:10.1890/1051-0761(1998)008[0559:NPOSWW]2.0.CO;2

Carreon-Martinez, L. B., K. W. Wellband, T. B. Johnson, S. A. Ludsin, and D. D. Heath. 2014. Novel molecular approach demonstrates that turbid river plumes reduce predation mortality on larval fish. Mol. Ecol. **23**: 5366–5377. doi:10.1111/mec.12927

Chen, Z., C. Hu, and F. Muller-Karger. 2007. Monitoring turbidity in Tampa Bay using MODIS/Aqua 250-m imagery. Remote Sens. Environ. **109**: 207–220. doi:10.1016/j.rse.2006.12.019

Dong, J., X. Xia, M. Wang, Y. Lai, P. Zhao, H. Dong, Y. Zhao, and J. Wen. 2015. Effect of water–sediment regulation of the Xiaolangdi Reservoir on the concentrations, bioavailability, and fluxes of PAHs in the middle and lower reaches of the Yellow River. J. Hydrol. **527**: 101–112. doi:10.1016/j.jhydrol.2015.04.052

Dong, J., X. Xia, M. Wang, H. Xie, J. Wen, and Y. Bao. 2016. Effect of recurrent sediment resuspension-deposition events on bioavailability of polycyclic aromatic hydrocarbons in aquatic environments. J. Hydrol. **540**: 934–946. doi:10.1016/j.jhydrol.2016.07.009

Fukuda, M. K., and W. Lick. 1980. The entrainment of cohesive sediments in freshwater. J. Geophys. Res. **85**: 2813–2824. doi:10.1029/JC085iC05p02813

Garel, E., L. Pinto, A. Santos, and Ó. Ferreira. 2009. Tidal and river discharge forcing upon water and sediment circulation at a rock-bound estuary (Guadiana estuary, Portugal). Estuar. Coast. Shelf Sci. **84**: 269–281. doi:10.1016/j.ecss.2009.07.002

Ge, J., F. Shen, W. Guo, C. Chen, and P. Ding. 2015. Estimation of critical shear stress for erosion in the Changjiang Estuary: A synergy research of observation, GOCI sensing and modeling. J. Geophys. Res. Oceans **120**: 8439–8465. doi:10.1002/2015JC010992

Green, M. O., and G. Coco. 2014. Review of wave-driven sediment resuspension and transport in estuaries. Rev. Geophys. **52**: 77–117. doi:10.1002/2013RG000437

Grimes, C. B., and J. H. Finucane. 1991. Spatial distribution and abundance of larval and juvenile fish, chlorophyll and macrozooplankton around the Mississippi River discharge plume, and the role of the plume in fish recruitment. Mar. Ecol. Prog. Ser. **75**: 109–119. doi:10.3354/meps075109

Grimes, C. B., and M. J. Kingsford. 1996. How do riverine plumes of different sizes influence fish larvae: Do they enhance recruitment? Mar. Freshw. Res. **47**: 191–208. doi:10.1071/MF9960191

Harris, C. K., C. R. Sherwood, R. P. Signell, A. J. Bever, and J. C. Warner. 2008. Sediment dispersal in the northwestern Adriatic Sea. J. Geophys. Res. **113**: C11S03. doi:10.1029/2006JC003868

Hawley, N., and B. J. Eadie. 2007. Observations of sediment transport in Lake Erie during the winter of 2004-2005. J. Great Lakes Res. **33**: 816–827. doi:10.3394/0380-1330(2007)33[816:OOSTIL]2.0.CO;2

Hawley, N., C. K. Harris, B. M. Lesht, and A. H. Clites. 2009. Sensitivity of a sediment transport model for Lake Michigan. J. Great Lakes Res. **35**: 560–576. doi:10.1016/j.jglr.2009.06.004

Islam, M. S., and M. Tanaka. 2004. Impacts of pollution on coastal and marine ecosystems including coastal and marine fisheries and approach for management: A review and synthesis. Mar. Pollut. Bull. **48**: 624–649. doi:10.1016/j.marpolbul.2003.12.004

Janssen, P. 1989. Wave-induced stress and the drag of air flow over sea waves. J. Phys. Oceanogr. **19**: 745–754. doi:10.1175/1520-0485(1989)019<0745:WISATD>2.0.CO;2

Janssen, P. 1991. Quasi-linear theory of wind-wave generation applied to wave forecasting. J. Phys. Oceanogr. **21**: 1631–1642. doi:10.1175/1520-0485(1991)021<1631:QLTOWW>2.0.CO;2

Jiang, L., M. Xia, S. A. Ludsin, E. S. Rutherford, D. M. Mason, J. M. Jarrin, and K. L. Pangle. 2015. Biophysical modeling

assessment of the drivers for plankton dynamics in dreissenid-colonized Western Lake Erie. Ecol. Model. **308**: 18–33. doi:10.1016/j.ecolmodel.2015.04.004

Jiang, L., and M. Xia. 2016. Dynamics of the Chesapeake Bay outflow plume: Realistic plume simulation and its seasonal and interannual variability. J. Geophys. Res. Oceans **121**: 1424–1445. doi:10.1002/2015JC011191

Lai, Z., R. Ma, M. Huang, C. Chen, Y. Chen, C. Xie, and R. C. Beardsley. 2016. Downwelling wind, tides, and estuarine plume dynamics. J. Geophys. Res. Oceans. **121**: 4245–4263. doi:10.1002/2015JC011475

Le, C., C. Hu, D. English, J. Cannizzaro, Z. Chen, L. Feng, R. Boler, and C. Kovach. 2013. Towards a long-term chlorophyll-a data record in a turbid estuary using MODIS observations. Prog. Oceanogr. **109**: 90–103. doi:10.1016/j.pocean.2012.10.002

Lee, D. Y., W. Lick, and S. W. Kang. 1981. The entrainment and deposition of fine-grained sediments in Lake Erie. J. Great Lakes Res. **7**: 224–233. doi:10.1016/S0380-1330(81)72049-5

Li, J., Y. Zhang, and S. Katsev. 2018. Phosphorus recycling in deeply oxygenated sediments in lake superior controlled by organic matter mineralization. Limnol. Oceanogr. **63**: 1372–1385. doi:10.1002/lno.10778

Lick, W., J. Lick, and C. K. Ziegler. 1994. The resuspension and transport of fine-grained sediments in Lake Erie. J. Great Lakes Res. **20**: 599–612. doi:10.1016/S0380-1330(94)71181-3

Liu, X., and M. Wang. 2014. River runoff effect on the suspended sediment property in the upper Chesapeake Bay using MODIS observations and ROMS simulations. J. Geophys. Res. Oceans **119**: 8646–8661. doi:10.1002/2014JC010081

Lou, J., D. J. Schwab, D. Beletsky, and N. Hawley. 2000. A model of sediment resuspension and transport dynamics in southern Lake Michigan. J. Geophys. Res. Oceans **105**: 6591–6610. doi:10.1029/1999JC900325

Ludsin, S. A., K. M. DeVanna, and R. E. Smith. 2014. Physical–biological coupling and the challenge of understanding fish recruitment in freshwater lakes. Can. J. Fish. Aquat. Sci. **71**: 775–794. doi:10.1139/cjfas-2013-0512

Madsen, O. S. 1994. Spectral wave–current bottom boundary layer flows. *In* Proceedings of the 24th International Conference on Coastal Engineering Research Council, Billy L. Edge, p. 384–398. American Society of Civil Engineers.

Mehta, A. J. 1986. Characterization of cohesive sediment properties and transport processes in estuaries. *In* A. J. Mehta [ed.], Estuarine cohesive sediment dynamics. Lecture notes on coastal and estuarine studies, v. **14**. p. 290–325. Springer.

Mellor, G. L. 2015. A combined derivation of the integrated and vertically resolved, coupled wave-current equations. J. Phys. Oceanogr. **45**: 1453–1463. doi:10.1175/JPO-D-14-0112.1

Mendes, R., G. S. Saldías, M. deCastro, M. Gómez-Gesteira, N. Vaz, and J. M. Dias. 2017. Seasonal and interannual variability of the Douro turbid river plume, northwestern Iberian Peninsula. Remote Sens. Environ. **194**: 401–411. doi:10.1016/j.rse.2017.04.001

Morales-Marin, L. A., J. R. French, H. Burningham, and R. W. Battarbee. 2017. Three-dimensional hydrodynamic and sediment transport modeling to test the sediment focusing hypothesis in upland lakes. Limnol. Oceanogr. **63**: S156–S176. doi:10.1002/lno.10729

Moriarty, J. M., C. K. Harris, K. Fennel, M. A. Friedrichs, K. Xu, and C. Rabouille. 2017. The roles of resuspension, diffusion and biogeochemical processes on oxygen dynamics offshore of the Rhône River, France: A numerical modeling study. Biogeosciences **14**: 1919–1946. doi:10.5194/bg-14-1919-2017

Niu, Q., M. Xia, E. S. Rutherford, D. M. Mason, E. J. Anderson, and D. J. Schwab. 2015. Investigation of interbasin exchange and interannual variability in Lake Erie using an unstructured-grid hydrodynamic model. J. Geophys. Res. Oceans **120**: 2212–2232. doi:10.1002/2014JC010457

Niu, Q., and M. Xia. 2016. Wave climatology of Lake Erie based on an unstructured-grid wave model. Ocean Dyn. **66**: 1271–1284. doi:10.1007/s10236-016-0982-7

Niu, Q., and M. Xia. 2017. The role of wave-current interaction in Lake Erie's seasonal and episodic dynamics. J. Geophys. Res. Oceans **122**: 7291–7311. doi:10.1002/2017JC012934

Paytan, A., K. Roberts, S. Watson, S. Peek, P. C. Chuang, D. Defforey, and C. Kendall. 2017. Internal loading of phosphate in Lake Erie Central Basin. Sci. Total Environ. **579**: 1356–1365. doi:10.1016/j.scitotenv.2016.11.133

Rabalais, N. N., and others. 2014. Eutrophication-driven deoxygenation in the coastal ocean. Oceanography **27**: 172–183. doi:10.5670/oceanog.2014.21

Reichert, J. M., B. J. Fryer, K. L. Pangle, T. B. Johnson, J. T. Tyson, A. B. Drelich, and S. A. Ludsin. 2010. River-plume use during the pelagic larval stage benefits recruitment of a lentic fish. Can. J. Fish. Aquat. Sci. **67**: 987–1004. doi:10.1139/F10-036

Saldías, G. S., M. Sobarzo, J. Largier, C. Moffat, and R. Letelier. 2012. Seasonal variability of turbid river plumes off Central Chile based on high-resolution MODIS imagery. Remote Sens. Environ. **123**: 220–233. doi:10.1016/j.rse.2012.03.010

Schwab, D. J., D. Beletsky, and J. Lou. 2000. The 1998 coastal turbidity plume in Lake Michigan. Estuar. Coast. Shelf Sci. **50**: 49–58. doi:10.1006/ecss.1999.0531

Schwab, D. J., D. Beletsky, J. DePinto, and D. M. Dolan. 2009. A hydrodynamic approach to modeling phosphorus distribution in Lake Erie. J. Great Lakes Res. **35**: 50–60. doi:10.1016/j.jglr.2008.09.003

Shen, F., Y. Zhou, J. Li, Q. He, and W. Verhoef. 2013. Remotely sensed variability of the suspended sediment concentration and its response to decreased river discharge in

the Yangtze estuary and adjacent coast. Cont. Shelf Res. **69**: 52–61. doi:10.1016/j.csr.2013.09.002

Sterner, R. W., P. Ostrom, N. E. Ostrom, J. V. Klump, A. D. Steinman, E. A. Dreelin, M. J. V. Zanden, and A. T. Fisk. 2017. Grand challenges for research in the Laurentian Great Lakes. Limnol. Oceanogr. **62**: 2510–2523. doi:10.1002/lno.10585

Thomas, R. L., J. M. Jaquet, A. L. W. Kemp, and C. F. M. Lewis. 1976. Surficial sediments of Lake Erie. J. Fish. Res. Board Can. **33**: 385–403. doi:10.1139/f76-061

Valipour, R., L. Boegman, D. Bouffard, and Y. R. Rao. 2017. Sediment resuspension mechanisms and their contributions to high-turbidity events in a large lake. Limnol. Oceanogr. **62**: 1045–1065. doi:10.1002/lno.10485

Wang, A., X. Ye, X. Du, and B. Zheng. 2014. Observations of cohesive sediment behaviors in the muddy area of the northern Taiwan Strait, China. Cont. Shelf Res. **90**: 60–69. doi:10.1016/j.csr.2014.04.002

Wu, K., M. Dai, X. Li, F. Meng, J. Chen, and J. Lin. 2017. Dynamics and production of dissolved organic carbon in a large continental shelf system under the influence of both river plume and coastal upwelling. Limnol. Oceanogr. **62**: 973–988. doi:10.1002/lno.10479

Xia, M., L. Xie, L. J. Pietrafesa, and M. M. Whitney. 2011. The ideal response of a Gulf of Mexico estuary plume to wind forcing: Its connection with salt flux and a Lagrangian view. J. Geophys. Res. **116**: C08035. doi:10.1029/2010JC006689

Xia, M., and L. Jiang. 2016. Application of an unstructured grid-based water quality model to Chesapeake Bay and its adjacent coastal ocean. J. Mar. Sci. Eng. **4**: 52. doi:10.3390/jmse4030052

Xia, X., and others. 2016. Effect of water-sediment regulation of the Xiaolangdi reservoir on the concentrations, characteristics, and fluxes of suspended sediment and organic carbon in the Yellow River. Sci. Total Environ. **571**: 487–497. doi:10.1016/j.scitotenv.2016.07.015

Yellen, B., J. D. Woodruff, D. K. Ralston, D. G. MacDonald, and D. S. Jones. 2017. Salt wedge dynamics lead to enhanced sediment trapping within side embayments in high-energy estuaries. J. Geophys. Res. Oceans **122**: 2226–2242. doi:10.1002/2016JC012595

Zamparas, M., and I. Zacharias. 2014. Restoration of eutrophic freshwater by managing internal nutrient loads. A review. Sci. Total Environ. **496**: 551–562. doi:10.1016/j.scitotenv.2014.07.076

Acknowledgments

This project is funded by the Great Lakes Fishery Commission's Fishery Research Program (GLFC-FRP; 2012_XIA_00421 to MX). Research was carried on the Computational and Information Systems Laboratory (CISL) Yellowstone (Support to M. Xia and Q. Niu) and Texas Advanced Computing Center (TACC) Stampede2 (Support to M. Xia). Research Data is archived at the National Center for Atmospheric Research, CISL, Boulder, Colorado. Surface forcing data was provided by the Great Lakes Environmental Research Laboratory (GLERL), National Oceanic and Atmospheric Administration (NOAA). Observational data for river input were obtained from the United States Geological Survey (USGS), the National Center for Water Quality Research (NCWQR) at Heidelberg College and the Water Survey of Canada (WSC). The MODIS true color images were derived from the Space Science and Engineering Center (SSEC) at University of Wisconsin-Madison. Additional observational data from Western Lake Erie (sites F01-F08) were provided by a GLFC-FRP project (GRT00012267 to SAL).

Conflict of Interest

None declared.

Submitted 8 January 2018
Revised 11 May 2018
Accepted 29 May 2018

Associate editor: Yong Liu